

Application of Coarse Integration to Bacterial Chemotaxis

S. Setayeshgar*,

Department of Physics, Princeton University, Princeton, NJ 08544

C. W. Gear,

*NEC Research Institute, 4 Independence Way, Princeton,
NJ 08540, and Department of Chemical Engineering,
Princeton University, Princeton, NJ 08544*

H. G. Othmer,

Department of Mathematics, University of Minnesota, Minneapolis, MN 55455

I. G. Kevrekidis

*Department of Chemical Engineering,
and Program in Applied and Computational Mathematics,
Princeton University, Princeton, NJ 08544*

(Dated: November 3, 2018)

Abstract

We have developed and implemented a numerical evolution scheme for a class of stochastic problems in which the temporal evolution occurs on widely-separated time scales, and for which the slow evolution can be described in terms of a small number of moments of an underlying probability distribution. We demonstrate this method via a numerical simulation of chemotaxis in a population of motile, independent bacteria swimming in a prescribed gradient of a chemoattractant. The microscopic stochastic model, which is simulated using a Monte Carlo method, uses a simplified deterministic model for excitation/adaptation in signal transduction, coupled to a realistic, stochastic description of the flagellar motor. We show that projective time integration of “coarse” variables can be carried out on time scales long compared to that of the microscopic dynamics. Our coarse description is based on the spatial cell density distribution. Thus we are assuming that the system “closes” on this variable so that it can be described on long time scales solely by the spatial cell density. Computationally the variables are the components of the density distribution expressed in terms of a few basis functions, given by the singular vectors of the spatial density distribution obtained from a sample Monte Carlo time evolution of the system. We present numerical results and analysis of errors in support of the efficacy of this time-integration scheme.

* Corresponding author. E-mail: simas@princeton.edu, Tel: (609) 258-4320, Fax: (609) 258-1549

I. INTRODUCTION

A recurring bottleneck in computational modeling of physical processes is the existence of multiple space and/or time scales. Important examples include patterns in fluids, defect dynamics in solids, and molecular dynamics of macromolecules. For example, in the latter case, the evolution of the physical configuration from initial to final state typically occurs on the time scale of milliseconds, while the interactions between constituent components must be resolved on the picosecond time scale. Furthermore, it is increasingly important in simulating biological systems to have a hybrid computational framework for interacting stochastic and deterministic processes, which occur on different time scales. Multiscale computational methods combine processing on fine space/time scales according to the governing microscopic description with macroscopic changes on a coarse grid (see for example, [1, 2, 3]).

Here we present a computational scheme for “coarse projective” time integration of the macroscopic dynamics of stochastic processes that involve multiple, widely-separated time scales. To illustrate the method we apply it to a microscopic model that generates the biased random walk describing the macroscopic motion of a bacterium such as *E. coli* in an attractant gradient. Details of this Monte Carlo model of bacterial chemotaxis that integrates signal transduction with the motor response are given in Section III. The focus of our analysis in this paper is the computational scheme, and as such, our results address its plausibility rather than the phenomenology of chemotaxis.

In Section II we discuss previous work on coarse time integration of microscopic dynamics and the new features of the method developed here, and we motivate its application to chemotaxis. The Monte Carlo description is presented in Section III. We outline the coarse integration scheme in Section IV, and present numerical results and analysis of errors in Section V. We conclude with future extensions and applications of this work.

II. PREVIOUS WORK

The traditional approach to studying long-term dynamics of multiscale processes involves (a) the derivation of a “coarse-grained” set of evolution equations, followed by, (b) the analytical and/or computational study of these reduced equations using established, continuum numerical analysis tools. Recently, a so-called “equation-free” approach to the study of the coarse-grained behavior of such problems has been proposed which circumvents the first step ([4, 5, 6]). This computational approach is based on the “coarse,” or macroscopic time-stepper, a map from the coarse variables at time $t = 0$ to those at time $t = T$, where T is typically much larger than characteristic microscopic time scales in the system. This map is not obtained directly from the macroscopic evolution equations, which we may not know, but rather through short time evolution intervals of appropriately initialized microscopic simulations. The initial macroscopic variables are *lifted* to microscopic variables to initialize the microscopic simulation. At the completion of a burst of microscopic simulation, the microscopic variables are *restricted* back to macroscopic variables, providing an approximation to the macroscopic time step. This provides a *chord* of the macroscopic solution, which is an approximation to the time derivative of the macroscopic solution. This value can then be used in any conventional continuum numerical method for the macroscopic equations. This approach has been applied in several microscopic contexts, and the results appear to be promising [7, 8, 9, 10].

In this work we apply the coarse timestepper in a projective integration study of a spatially-distributed kinetic Monte Carlo simulation of a biased random walk. When, as in this case, the microscopic equations are stochastic, an effective algorithm must reduce the variance inherent in individual realizations of the stochastic process to a level that can be tolerated by the continuum numerical algorithm applied to the coarse system. This can be done by lifting to multiple copies, or, as is done here, by estimating the derivative from a least-squares fit to a large number of microscopic time steps. The projective integration method applied here uses a derivative estimate for the projective step, so that the stochastic noise is amplified by the inverse of the effective step length used in the derivative estimate. Hence, variance reduction is very important. Augmenting the number of copies of the simulation (which, for our noninteracting particle model corresponds also to a simulation with a larger number of cells) is the most direct approach to variance reduction; other variance reduction schemes are discussed in [11, 12].

In the context of bacterial chemotaxis, the computational scheme developed here can be viewed as a direct method to compute the macroscopic evolution of the cell density in space and time without actually deriving these equations. An alternate approach begins with the transport equation for the velocity jump process, in which discontinuous changes in the direction (or speed) of an individual cell are generated by a Poisson process. It can be shown rigorously that this reduces to the chemotaxis equation under suitable scaling of space and time [13]

$$\frac{\partial \mu_0}{\partial t} = \nabla \cdot (D \nabla \mu_0 - \mu_0 \chi(S) \nabla S), \quad (1)$$

In the above, $\mu_0(x, t)$ represents the density of particles at spatial position x at time t , D is the diffusion constant, S is the concentration of the chemotactic attractant/repellent, and $\chi(S)$ is the chemotactic sensitivity. However, there is as yet no analytical procedure available for determining the diffusion constant and chemotactic sensitivity when dependence on internal state variables determining the cell's response to the external signal is explicitly included the transport equation. We show that a macroscopic time-stepper can be used here in the time evolution of the spatial density, even though the macroscopic evolution equations are not known.

III. BACTERIAL CHEMOTAXIS

A. Signal transduction

The ability to sense and respond to environmental cues is necessary for the survival of most organisms. *Escherichia Coli* (*E. coli*) is a common and well-known single cell organism, with roughly 4000 genes, whose chemotaxis network has emerged as a prototype for understanding signal transduction networks in general [14]. Its genome is known, the crystal structures of many proteins have been obtained, and a large number of mutant strains exist, allowing detailed behavioral studies.

For each cell, chemotactic behavior begins when attractant or repellent molecules bind to membrane receptors, triggering a cascade of chemical reactions inside the cell that culminates in the production of the phosphorylated form of a response regulator protein (CheY-P) which controls the direction of rotation of the flagellar motor. The series of reactions that converts the extracellular signal (attractant/repellent) into cellular response is referred to

as the signal transduction pathway. Flagella possess an inherent chirality, such that counter-clockwise (CCW) rotation results in bundling-up of the six to eight flagella per cell, allowing them to act as a single propeller and leading to smooth swimming motion of the bacterium. When the flagella rotate clockwise (CW), the bundle flies apart and the bacterium tumbles. As conditions become increasingly favorable due to increase in chemoattractant concentration, a bacterium extends its run-length; otherwise, it tumbles, and the subsequent direction of motion is randomly chosen, allowing a more favorable direction to be discovered. The resulting motion is a biased random walk toward favorable conditions and away from less favorable ones.

The sequence of biochemical reactions that take place inside a bacterium, starting with the binding of an attractant or repellent molecule to receptors on the cell surface and leading to the change in concentration of the response regulator species, CheY-P, has been extensively studied. Both deterministic models of these biochemical pathways, based on the law of mass action and Michaelis-Menten kinetics [15, 16], as well as fully stochastic models exist [17]. Measurement of concentration change is achieved through a temporal rather than a spatial comparison: fast sampling of the present external concentration is compared with memory of that concentration some time ago. Order-of-magnitude analyses for why measurement of concentration changes as spatial gradients across the cell length is not physically feasible have been given [18].

Memory in the signal transduction network is achieved through the existence of fast and slow reaction time scales. The fast reactions are receptor-ligand binding and phosphorylation kinetics; the slow reactions are methylation and demethylation. Ligand binding reduces the autophosphorylation rate of the corresponding membrane-bound receptor, in turn decreasing the rate of transfer of phosphoryl groups to CheY, and resulting in a (fast) drop in [CheY-P]. Addition of methyl groups to ligand-bound receptors restores the autophosphorylation rate, resulting in (slow) increase in [CheY-P]. The rate of demethylation becomes significant once a high methylation level is achieved. Hence, [CheY-P] reflects the balance between the fraction of ligand-bound receptors and methylated receptors. Perfect adaptation refers to the return of [CheY-P] to the same steady state level, regardless of the constant concentration level of the external stimulus. This value falls within the fixed operational range of the motor response to CheY-P.

A minimal model representing the signal transduction process includes fast excitation and slow adaptation to an external stimulus and is given in [19]:

$$\frac{du_1}{dt} = \frac{(f(S) - u_2) - u_1}{\tau_e}, \quad (2)$$

$$\frac{du_2}{dt} = \frac{f(S) - u_2}{\tau_a}, \quad (3)$$

where τ_e and τ_a are the excitation and adaptation times, respectively, with $\tau_e \ll \tau_a$. We identify u_1 with the deviation of [CheY-P] from its steady state value, and u_2 as the number of methylated receptors per unit volume. $f(S) = f(S(t))$ is a function of the external stimulus; for example, it is the number of bound receptors per unit volume in the presence of an external signal concentration, S :

$$f = N_T S / (K_L + S). \quad (4)$$

N_T is the total number of receptors per unit volume, and K_L is the dissociation constant for the ligand-binding process.

The formal solution to Eqs. (2)–(3) can be easily obtained for each cell as

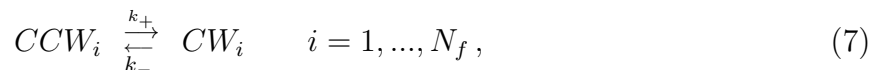
$$u_2(t) = \frac{e^{-t/\tau_a}}{\tau_a} \int^t f(S(t')) e^{t'/\tau_a} dt', \quad (5)$$

$$u_1(t) = \frac{e^{-t/\tau_e}}{\tau_e} \left(\int^t f(S(t')) e^{t'/\tau_e} dt' - \frac{1}{\tau_a} \int^t e^{-t'(1/\tau_a - 1/\tau_e)} \int^{t'} f(S(t'')) e^{t''/\tau_a} dt'' dt' \right). \quad (6)$$

However, because $S(t) = S(x(t), t)$, where $x(t)$ is a random variable that represents the cell's position at time t in a given external concentration field, the integration takes place along the cell trajectory, which is a biased random walk: $x(t')$ for $t' < t$ biases the probability of $x(t)$. Hence, $S(t)$ is a stochastic variable, and the integration must be carried out computationally.

B. Motor and cell response

We adopt a stochastic approach to modeling the response of the flagellar motor to the regulator species, CheY-P. The motor is assumed to be in one of two states, CW or CCW, corresponding to clockwise or counterclockwise rotation [20, 21]. The rates of transition between these states are functions of [CheY-P]:



where N_f is the number of flagella per cell. For any concentration of CheY-P, the motor has a nonzero probability of being in either state. The probability of waiting at least a time T for a transition from CCW to CW, Φ_+ , or a transition from CW to CCW, Φ_- , is given by:

$$\Phi_{\pm} = e^{-\int_0^T k_{\pm}(t) dt}. \quad (8)$$

If the motor is probed at a time $T \equiv \Delta t$, such that $k_{\pm} \Delta t \ll 1$, then the probability that a change in direction will occur in $(T, T + \Delta t)$ can be approximated as

$$1 - \Phi_{\pm} \approx k_{\pm}(0) \Delta t. \quad (9)$$

Systematic studies have been undertaken that show simulation results are qualitatively independent of the choice of Δt once the above restrictions are met.

In this work, we use equilibrium transition rates, k_{\pm} , consistent with recent experimental measurements [22] of the single flagellum clockwise bias, b_{CW} , and the reversal frequency, w , as functions of [CheY-P]. The rates are related to these measured quantities according to [23]:

$$b_{CW} = \frac{k_+}{k_+ + k_-}, \quad (10)$$

$$w = \frac{2k_+ k_-}{k_+ + k_-}, \quad (11)$$

where the reversal frequency is the geometric mean of the transition rates. We take b_{CW} to be described by a Hill function, $b_{CW} = y_p^h / (K_M^h + y_p^h)$, where $y_p = [\text{CheY} - \text{P}]$, with experimentally measured values for the Hill coefficient and dissociation constant, equal to

$h = 10.3$ and $K_M = 3.1 \mu\text{M}$. In these experiments, it was noted that the data were consistent with $w = (2 \mu\text{M s}^{-1}) \partial b_{CCW} / \partial y_p$. Based on these results, we use

$$k_+ = \frac{h y_p^{h-1}}{K_M^h + y_p^h}, \quad (12)$$

$$k_- = \frac{1}{y_p} \frac{h K_M^h}{K_M^h + y_p^h}. \quad (13)$$

In a constant chemoattractant field, [16, 24] show that the ‘‘Voting Hypothesis’’ is successful in producing the correct running bias of the cell, B_{CCW} , from the individual flagellar bias, b_{CCW} :

$$B_{CCW} = \sum_{j=\nu}^{N_f} \binom{N_f}{j} b_{CCW}^j (1 - b_{CCW})^{N_f-j}, \quad (14)$$

where ν is the minimum number of flagella required to be in the CCW state for the cell to run. Although cooperativity among the flagella is not yet fully understood, we similarly adopt the ‘‘majority rules’’ algorithm to determine whether each cell will run or tumble in the presence of a chemoattractant gradient:

$$\nu = \sum_{i=1}^{N_f} s^{(i)}. \quad (15)$$

where $s^{(i)} = 0, 1$ is the state of the i^{th} flagellum, corresponding to CW and CCW directions of rotation, respectively. Based on the experimentally measured gain of a single flagellum [22], a steady state value of $\bar{y}_p = 2.95 \mu\text{M}$ yields $b_{CCW} \sim 0.64$ to within experimental error. The resulting running bias for the cell, according to Eq. 14, is $B_{CCW} \sim 0.86$ for $N_f = 6$ and $\nu = 3$, in agreement with experimental results. Hence, if three or more flagella are determined to be in the CCW state, the cell in our simulation runs; otherwise, it tumbles.

C. Monte Carlo scheme

For each cell, the Monte Carlo scheme can be outlined as follows. At t_n :

- (a) Each flagellum has a state s_n , where $s_n = 0$ if CW, and $s_n = 1$ if CCW. To determine s_{n+1} , for each flagellum, we draw a uniformly distributed random number, $\zeta \in [0, 1]$.
- (b) We determine an approximation to the probability for changing direction of rotation, given by Eq. 9. If the values of k_{\pm} are such that this approximation is not valid, Δt is reduced until it is. This probability is a function of [CheY-P], which depends on the trajectory that the cell has taken along the external chemoattractant gradient.
 - If the flagellum is in the CW state ($s_n = 0$) and $\zeta < k_- \Delta t$, it continues in the CW state ($s_{n+1} = 0$); else, it switches to the CCW state ($s_{n+1} = 1$).
 - If the flagellum is in the CCW state ($s_n = 1$) and $\zeta < k_+ \Delta t$, it continues in the CCW state ($s_{n+1} = 1$); else, it switches to the CW state ($s_{n+1} = 0$).

- (c) If three or more flagella are now in the CCW state, $\nu_{n+1} \geq 3$ in Eq. 15, and the cell runs; else, it tumbles. If the cell is determined to run and $\nu_n < 3$, the direction of motion is chosen to be left or right with equal probability. Otherwise, it continues to run in the same direction.
- (d) The position of the j^{th} cell, $x_n(j)$, is accordingly updated to $x_{n+1}(j)$ (using the accepted time step Δt), with the cell speed, v_{cell} , assumed to be constant and independent of position.
- (e) The signal transduction variables (u_1, u_2) are integrated in time, using the forward Euler scheme. Their time history is a function of each cell's trajectory.

D. Combining signal transduction and motor response

Although we use a toy excitation-adaptation model to describe signal transduction, it is coupled to an experimentally realistic description of the flagellar switch. To do so requires introducing (i) a shift in the steady state value of u_1 , and (ii) an amplification or gain factor, g_0 , for the signal transduction network, required so that the output of this network spans the dynamic range of the motor:

$$y_p = \bar{y}_p - g_0 u_1 \quad (16)$$

The issue of gain in chemotaxis continues to receive much attention [25]. Given the level of simplicity of our signal transduction model, we do not imply this treatment of network gain to be physically realistic. An obvious drawback is that, like other parameters in the toy model (excitation and adaptation times), it is static, whereas in the actual biological system, these parameters depend on the external signal.

In Table I, we report the numerical values for the MC model parameters that operationally interface the toy signal transduction model with the realistic model of the flagellar switch. Hence, although the choice of toy model parameters was “physically motivated”, we do not attempt to make direct correspondence with experimental values. We caution the reader against making quantitative connection between our numerical results at these values and experimental results.

TABLE I: Numerical values for parameters used in the Monte Carlo evolution.

Parameter	Value
τ_a	100 s
τ_e	0.1 s
g_0	5
N_T	15 μM
K_L	1 μM
\bar{y}_p	2.95 μM
K_M	3.1 μM
v_{cell}	20 $\mu\text{m s}^{-1}$

IV. COARSE INTEGRATION

For the present problem of simulating the chemotactic response of a population of independent bacteria, the microscopic phase space is a directproduct of the phase space for each cell, consisting of its

- signal transduction variables: $\vec{u} = (u_1, u_2)$,
- flagellar state: \vec{s} , where $s^{(i)} = 0, 1$ for $i = 1 \dots N_f$,
- position: x ,
- direction of motion, $d = R, L, T$, corresponding to running right, running left and tumbling, respectively.

Rather than evolving all microscopic degrees of freedom, a coarse integration scheme identifies suitable reduced variable(s) to be integrated. A clearly relevant reduced variable in population studies is the spatial density distribution of cell positions, $\mu_0(x, t)$, obtained from the set of individual cell positions, x_j , which are a subset of the full microscopic phase space. However, it is possible that the unknown equations of the coarse description use additional variables, for example, the densities of the right moving, left moving, and tumbling cells, ρ_i where $i = R, L$, or T . In this case, $\mu_0(x, t) = \sum_i \rho_i(x, t)$. Indeed, an optimal reduced representation balances accuracy and efficiency of modeling the physical process. Here, we propose to retain only the spatial density distribution $\mu_0(x, t)$ as the relevant macroscopic variable in coarse modeling of chemotaxis since, as we will demonstrate numerically, the density of cells in each state rapidly approaches a functional of the total density.

A systematic approach to testing the adequacy of a particular coarse description is discussed in [9]. It is based on locating the same fixed point at different levels of coarse description, and examining the slow eigenvalues and corresponding eigenvectors of the linearization of the coarse timestepper at these fixed points (see also the discussion in [7]).

The separation of characteristic time scales describing the underlying macroscopic and microscopic dynamics – for example, the (long) time scale on which the spatial density distribution of a population of bacteria moving in a chemoattractant profile changes versus the (short) mean runtime of a single cell – allows taking time steps in evolving the macroscopic state that are “long” in comparison with the “fast” microscopic time scales in the problem, resulting in a computationally - efficient time evolution of the macroscopic state. We demonstrate this assumption of the separation of time scales explicitly in Section V. Figure 1 shows a cartoon sketch of the *coarse integration* (CI) procedure, where the solid trajectories denote the *restriction* of the full dynamics onto a suitable low-dimensional subspace (see Section IV A for how a low dimensional representation of the macroscopic spatial distribution, $\mu_0(x, t)$, is constructed). At each CI step, the coarse-integrated solution is *lifted* from the lower dimensional space into the full microscopic state space and evolved according to the Monte Carlo scheme, allowing the error incurred during the coarse time step to relax to the slow manifold parameterized by the cell density. Because the internal state $\{\vec{u}, \vec{s}\}$ of cells, and their directions of motion, d , are ignored in obtaining $\mu_0(x, t)$, they must be suitably reinitialized to construct the initial condition for the next MC step (see Section IV B).

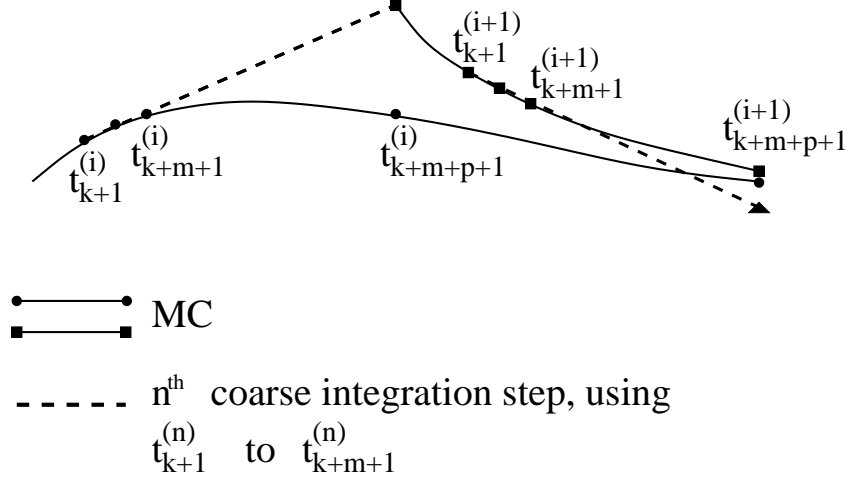


FIG. 1: Schematic illustration of the coarse integration procedure.

A. SVD-based restriction scheme

Below, we outline our coarse integration scheme which operates on data from singular value decomposition of the distribution of cell positions from Monte Carlo time evolution results. In the following, the solution at a “reporting step” refers to the sorted cell positions at specified time intervals, T_{step} . Note that this time interval should be distinguished from a single Monte Carlo iteration, of which it contains a large number.

1. The Monte Carlo description is simulated for k reporting steps, corresponding to a total time interval equal to T_{settle} . Step by step results are accumulated for a further m reporting steps, corresponding to a total time interval equal to T_{fit} .
2. At each reporting step, we sort the cell positions, $x_i(j)$, to obtain $X_i(j)$, $i = k + 1, \dots, k + m$, and $j = 1, \dots, N_{cells}$. The matrix A_ℓ is constructed (columnwise): $A_\ell = \{\vec{X}_{k+1}, \vec{X}_{k+2}, \dots, \vec{X}_{k+m}\}$. Figures 2 and 3 show the chemoattractant profile, and representative time sequences of sorted cell positions and corresponding histograms of the spatial density distributions, respectively. However, we find it more convenient to work with the cumulative probability distribution function, defined as

$$P(X, t) = \frac{1}{L} \int_{x_{min}}^X \mu_0(x', t) dx', \quad (17)$$

which is related to the sorted cell positions at that time according to

$$j/N_{cells} = P(X_i(j), t_i), \quad (18)$$

where $L \equiv x_{max} - x_{min}$ is the spatial domain. We will use approximations to $P(X, t)$, or equivalently the sorted cell positions, \vec{X}_i , as the macroscopic variable [26].

3. A low dimensional representation of the sorted cell positions is constructed in terms of orthonormal numerical basis functions, $\{\vec{u}^{(r)}\}$,

$$\alpha^{(r)}(t_i) = \vec{u}^{(r)} \cdot \vec{X}_i = \sum_{j=1}^{N_{cells}} u^{(r)}(j) X_i(j), \quad (19)$$

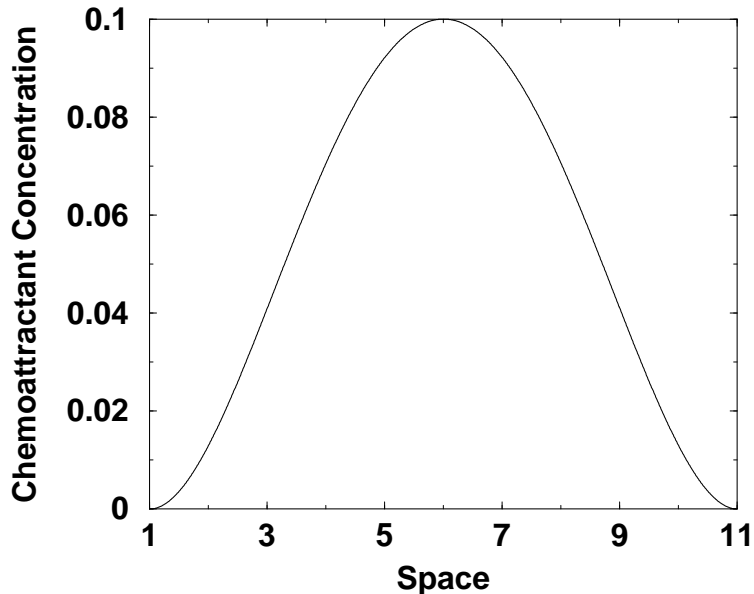


FIG. 2: Chemoattractant profile used in Monte Carlo simulation of chemotaxis: $S(x) = S_0(x - x_{min})^2(x - x_{max})^2$, where $S_0 = 1.6 \times 10^{-4}$ and $(x_{min}, x_{max}) = (1, 11)$. The choice of this profile ensures zero gradient of chemoattractant at the boundaries, consistent with no-flux boundary conditions for the motion of bacteria.

where the basis functions are obtained from singular value decomposition of the MC data as described below.

We distinguish between two approaches to obtaining the numerical basis set.

- *Local basis functions:* The singular value decomposition of A_ℓ , constructed in Step 2, is computed:

$$A_\ell = U_\ell W_\ell V_\ell^\top \quad (20)$$

The columns of U_ℓ , given by $\{\vec{u}_\ell^{(r)}\}$, $r = 1, \dots, m$, are the numerical basis functions. We assume that they remain valid basis functions during the projected step. W_ℓ is a diagonal matrix, where $\{w_{\ell 1}, w_{\ell 2}, \dots, w_{\ell m}\}$ are the singular values.

- *Global basis functions:* Using a single MC evolution from initial conditions to steady state, T_f , the matrix A_g is constructed from the full data according to Step 2: $A_g = \{\vec{X}_1, \vec{X}_2, \dots, \vec{X}_M\}$, where $M = T_f/T_{step}$. Singular value decomposition of A_g gives the the global basis functions, $\{\vec{u}_g^{(r)}\}$. (In practice, initial data from $t = 0$ to $t = T_{settle}$ are not included.)

4. We perform linear least squares extrapolation of $\{\alpha^{(r)}(t_i)\}$ using $i = k+1, \dots, k+m+1$ to obtain $\{\alpha^{(r)}(t_{k+m+1+p})\}$, corresponding to a projected time equal to T_{proj} . The projected solution is given by:

$$\vec{Y}_{k+1+m+p} = \sum_r \alpha^{(r)}(t_{k+m+1+p}) \vec{u}^{(r)}. \quad (21)$$

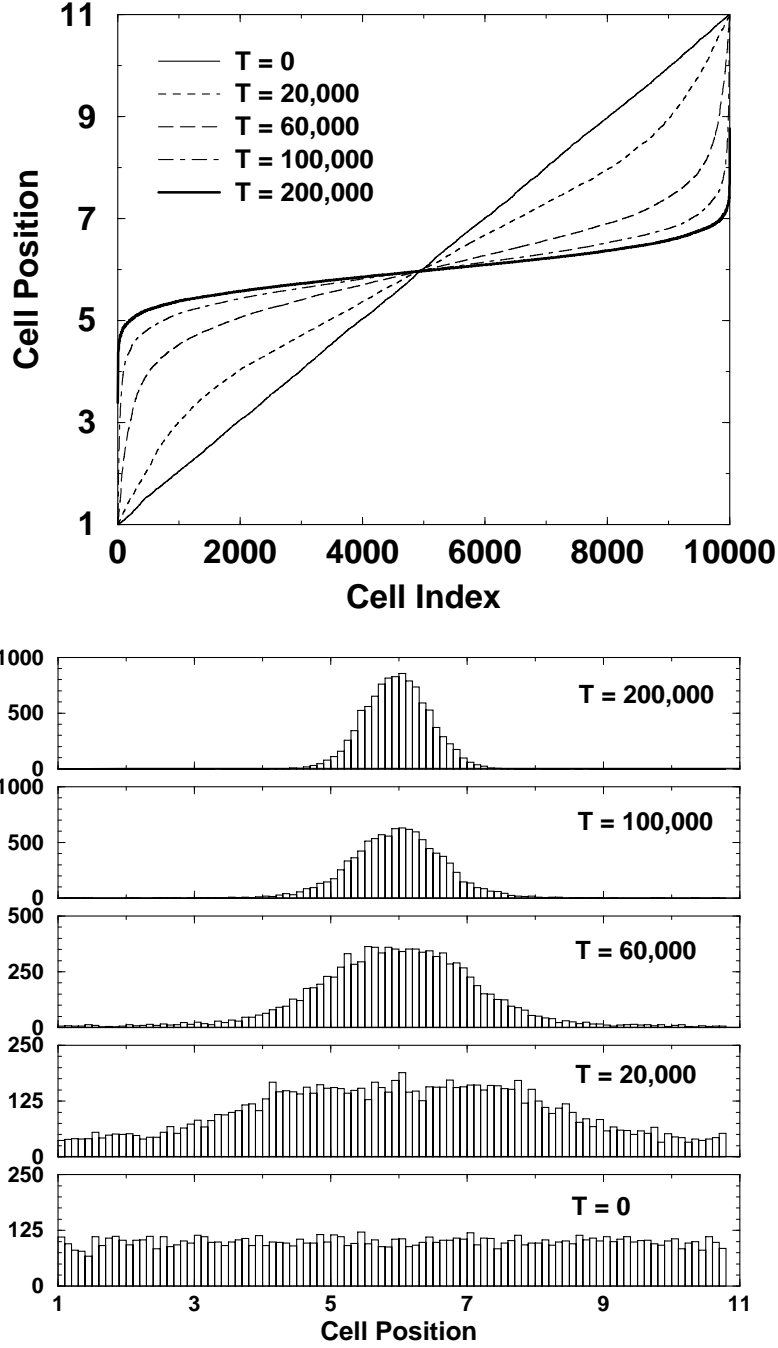


FIG. 3: Sorted cell positions (top), and corresponding histograms (bottom) using a bin size equal to 0.1, at $T = 0$ (thin solid line), $T = 20,000$ (dashed line), $T = 60,000$ (long-dashed line) and $T = 100,000$ (dot-dashed line), and $T = 200,000$ (thick solid line). From the time evolution of the variance of these distributions we have determined that at $T = 200,000$, the coarse solution is very close to the stationary state.

5. In practice, we use only the numerical basis functions associated with the dominant singular values, $r = 1, \dots, r_{max}$, where the truncated number of basis functions, r_{max} , depends on the spectrum of singular values.

The use of empirical orthogonal eigenfunctions, also referred to as the Karhunen-Loève expansion or the Proper Orthogonal Decomposition, obtained through singular value decomposition of experimental or simulation data, for model reduction in systems with spatiotemporal dynamics originates with Lorenz in the context of weather prediction [27] and has found widespread use in the dynamical systems context since the mid-80's (see the monograph [28] and references therein).

The SVD process is computationally expensive, so if the computational cost of the microscopic cell simulations were small, using global basis functions generated in a preliminary run would be less costly than using local basis functions. However, in a simulation of a large number of cells, the total microscopic simulation cost for the cell population may be much larger than for the SVD process. For example, in the numerical experiments reported here the CPU time for one simulation step of an individual cell was 2.07 microseconds, while the time for one SVD step was 22.4 milliseconds. However, in a simulation of 10^4 cells using local basis functions, the microscopic integration routine was called 4×10^9 times versus 16 calls on the SVD routine so that 0.0041% of the time was spent on SVD.

B. Reinitialization of internal variables

The question of consistent schemes for combining microscopic and macroscopic descriptions of a physical process is central to multiscale modeling. Here, to alternate each CI step with MC, in principle allowing relaxation of the numerical error in the projective step, we must define an appropriate reinitialization procedure: We know the position of each cell, x , after the CI step, but we discard all information about its internal state, $\{\vec{u}, \vec{s}\}$, given by the values of the signal transduction variables and the flagellar states, and its direction of motion, d_j .

Our reinitialization protocol is empirically motivated: the signal transduction variables are set equal to their local equilibrium values, $\vec{u}_j = \{0, f(S(x_j))\}$, where j refers to the j^{th} cell. This allows the subsequent response of each cell to be within the most sensitive range of the motor gain. For simplicity, all (six) flagella are restarted in the CW state, $\vec{s}_j = \{0, 0, \dots, 0\}$. In Figure 4, we show relaxation of the ratios of the numbers of right, left and tumbling cells at a set location along the chemoattractant profile. These ratios at steady state for a flat chemoattractant profile are

$$\frac{\rho_R + \rho_L}{\mu_0} = B, \tag{22}$$

where the right and left moving ratios are equal. For the present choice of numerical parameters, $B \sim 0.86$ and $\rho_R = \rho_L \sim 0.43$. Other flagellar reinitialization schemes lead to similarly rapid relaxation rates.

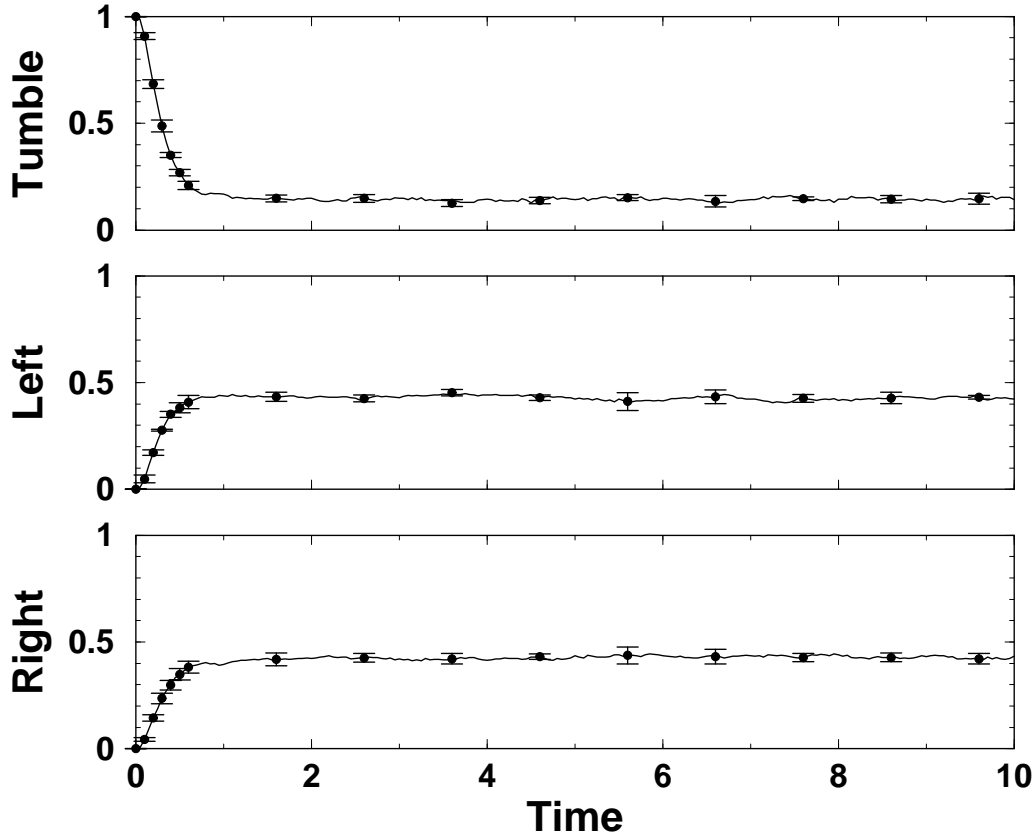


FIG. 4: Ratios of right moving, left moving and tumbling cells at $x = 4(\pm 0.1)$, using $j = 1, \dots, N_{cells} = 100,000$ and starting from an initially uniform distribution of cells along the chemoattractant profile: Averages over 5 Monte-Carlo realizations started from different random number seeds are plotted. The error bars, corresponding to the root-mean-square of the distribution of these ratios, are shown for select points. We note fast relaxation of these ratios to their equilibrium values. The signal transduction variables were initialized to their local equilibrium values, $\vec{u}_j = \{0, f(S(x_j))\}$.

V. NUMERICAL RESULTS

A. Low-dimensional representation

In Figures 5 and 6, we show the first four dominant global basis functions and singular values obtained from MC evolution of $N_{cells} = 10^4$ from initial conditions to steady state. Figure 7 shows the mean coefficients over $N_{MC} = 10$ MC realizations

$$\bar{\alpha}^{(r)}(t) = \frac{1}{N_{MC}} \sum_{k=1}^{N_{MC}} \alpha_k^{(r)}(t), \quad (23)$$

and the root-mean-square of the distribution of coefficients, given by

$$\sigma_{\alpha}^{(r)}(t) = \left\{ \frac{1}{N_{\text{MC}} - 1} \sum_{k=1}^{N_{\text{MC}}} [\alpha_k^{(r)}(t) - \bar{\alpha}^{(r)}(t)]^2 \right\}^{1/2}. \quad (24)$$

Hence, the error bars in this figure denote the expected statistical variation in the values of these coefficients as a function of time.

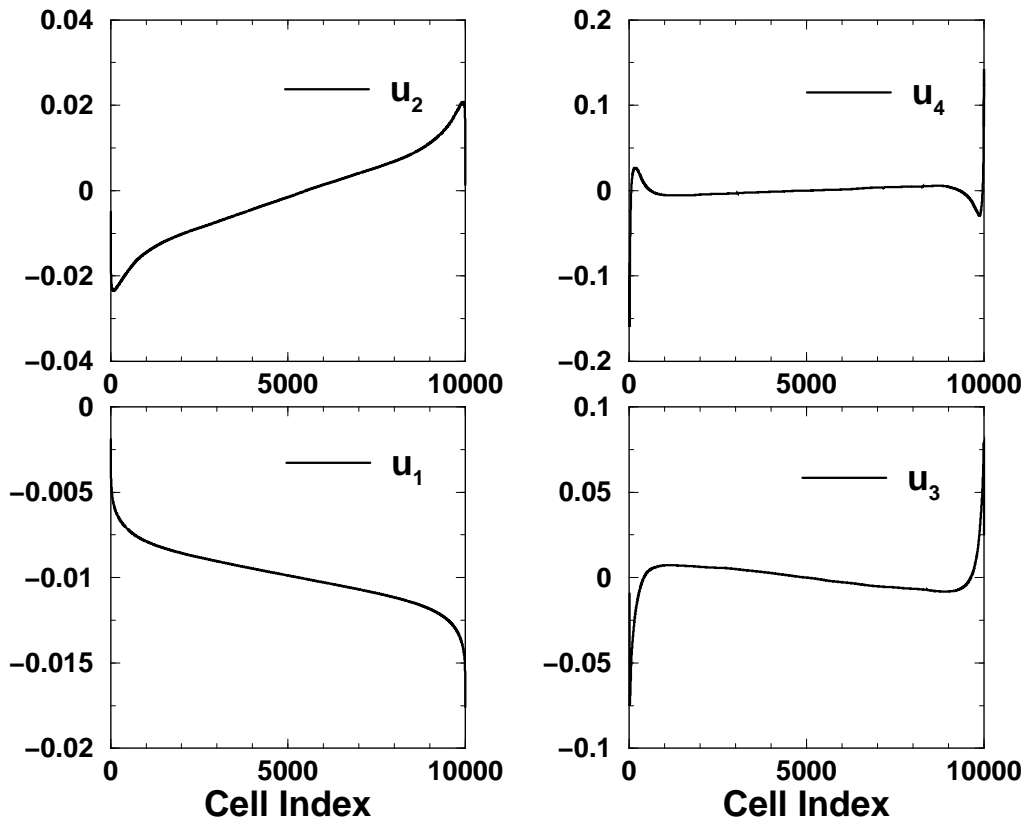


FIG. 5: $\{\bar{u}_g^{(r)}\}$, $r = 1, \dots, 4$ are the first four global SVD basis functions for the cumulative cell density.

In Figure 8, we show the low-dimensional representation of the coarse-integrated solution for $T_{\text{settle}} = T_{\text{fit}} = 5 \times 10^2$ and $T_{\text{proj}} = 5 \times 10^3$. For each CI step, after evolving the Monte Carlo for T_{settle} , we use a linear fit to $\{\alpha^{(1)}(t), \alpha^{(2)}(t), \alpha^{(3)}(t), \alpha^{(4)}(t)\}$ during the interval T_{fit} to project the solution forward in time by T_{proj} . The points correspond to averages over $N_{\text{MC}} = 5$ realizations, and the error bars give the rms of the distribution of these coefficients. For reference, we have included the average MC coefficients in this figure. These results indicate that for the higher order coefficients, $\{\alpha^{(3)}(t), \alpha^{(4)}(t)\}$, whose coarse dynamics are described by a shorter characteristic time-scale, a higher order time integration scheme would be more effective than the explicit Euler method used here [29]. Consequently, although for intermediate times the difference between the CI and MC results the straightforward CI scheme has captured the macroscopic dynamics of the solution.

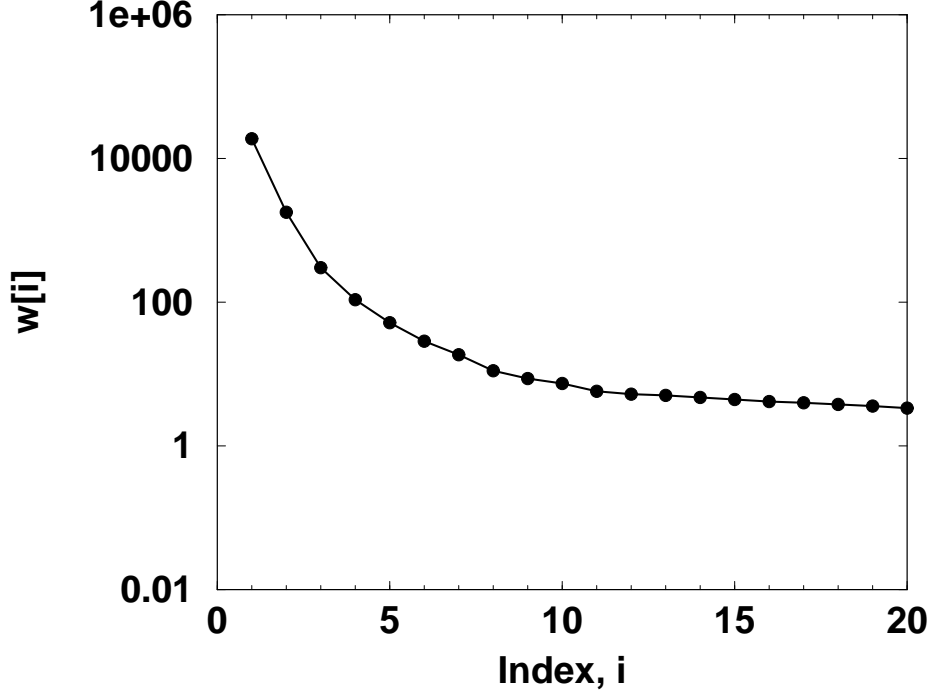


FIG. 6: Largest singular values from global SVD of Monte Carlo data from initial conditions to steady state ($T_f = 200,000, T_{step} = 200$). The first four dominant modes ($r_{max} = 4$) are used to construct the low-dimensional representation of the cumulative cell density distribution.

These results also illustrate the implicit assumption of separation of time scales: The coefficients $\{\alpha^{(r)}(t)\}$, governing the macroscopic behavior of the system, vary on a time scale of $\mathcal{O}(10^4)$ units, while the longest microscopic time scale (adaptation time of the signal transduction model) is $\mathcal{O}(10^2)$.

B. Analysis of Errors

For comparison of solutions at different values of the CI parameters, ($T_{settle}, T_{fit}, T_{proj}$), with the MC, we construct the following measure of relative error:

$$\varepsilon(t) = \left\{ \frac{\sum_{r=1}^4 [\alpha^{(r)}(t) - \bar{\alpha}^{(r)}(t)]^2}{\sum_{r=1}^4 [\bar{\alpha}^{(r)}(t)]^2} \right\}^{1/2}. \quad (25)$$

The coefficients $\{\alpha^{(1)}(t), \alpha^{(2)}(t), \alpha^{(3)}(t), \alpha^{(4)}(t)\}$, used in computing the relative error of the CI solution are obtained as inner products of the solution with the global basis set, regardless (a) of whether global or local basis sets were used in the restricting/lifting step, and (b) the dimensionality of the restricted space.

In Figure 9, we first plot the average relative error for $N_{MC} = 10$ MC runs, given by:

$$\bar{\varepsilon}(t) = \frac{1}{N_{MC}} \sum_{k=1}^{N_{MC}} \varepsilon_k(t). \quad (26)$$

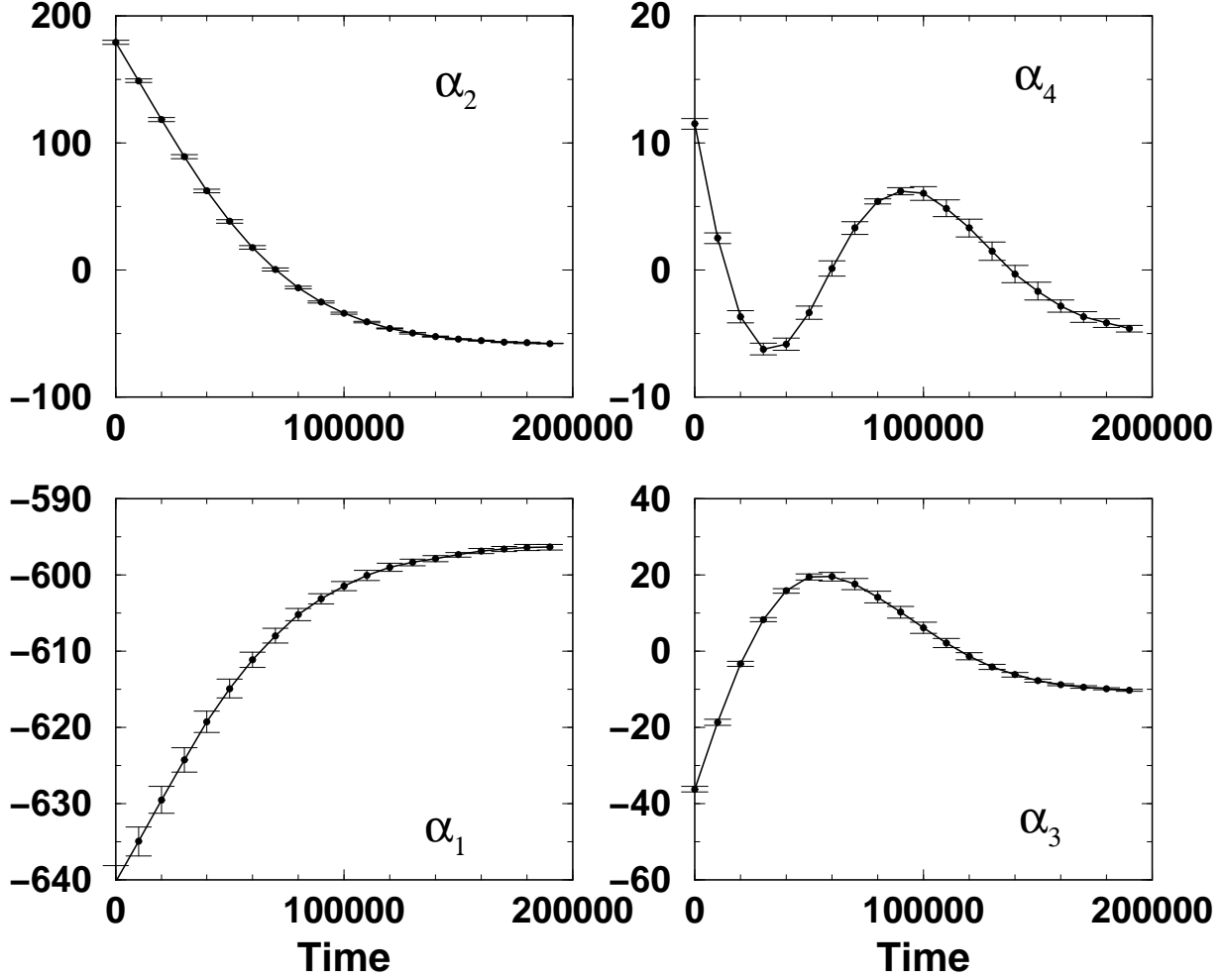


FIG. 7: Coefficients of SVD basis functions: $\alpha^{(r)}(t_i) = \vec{u}^{(r)} \cdot \vec{X}_i = \sum_{j=1}^{N_{cells}} u^{(r)}(j) X_i(j)$, where the points represent averages over $N_{MC} = 10$ MC realizations, starting from different random number seeds. The global basis functions $\{\vec{u}^{(r)}\}$ are obtained from one of the MC runs. The error bars, plotted for select points, correspond to the root-mean-square of the distribution of coefficients.

The error bars denote the error on the mean, given by $\sigma_{\bar{\varepsilon}} = \sigma_{\varepsilon} / \sqrt{N_{MC}}$, where σ_{ε} is the root-mean-square of the distribution of the error

$$\sigma_{\varepsilon}(t) = \left\{ \frac{1}{N_{MC} - 1} \sum_{k=1}^{N_{MC}} [\varepsilon_k(t) - \bar{\varepsilon}(t)]^2 \right\}^{1/2}. \quad (27)$$

We similarly compute the relative error for CI solutions, obtained using either (i) global or (ii) local SVD basis functions in each step. Figure 10 shows the mean errors for solutions with CI parameters given by $(T_{settle}, T_{fit}, T_{proj}) = 10^3 \times (\frac{1}{2}, \frac{1}{2}, 5)$, $10^3 \times (1, 1, 10)$ and $10^3 \times (2, 2, 20)$. Note that for these parameter values, the efficiency of the CI scheme remains the same. In this figure, solid lines show results obtained using global SVD basis functions, $\{\vec{u}_g^{(1)}, \vec{u}_g^{(2)}, \vec{u}_g^{(3)}, \vec{u}_g^{(4)}\}$, in the CI steps. Dashed lines show these results obtained

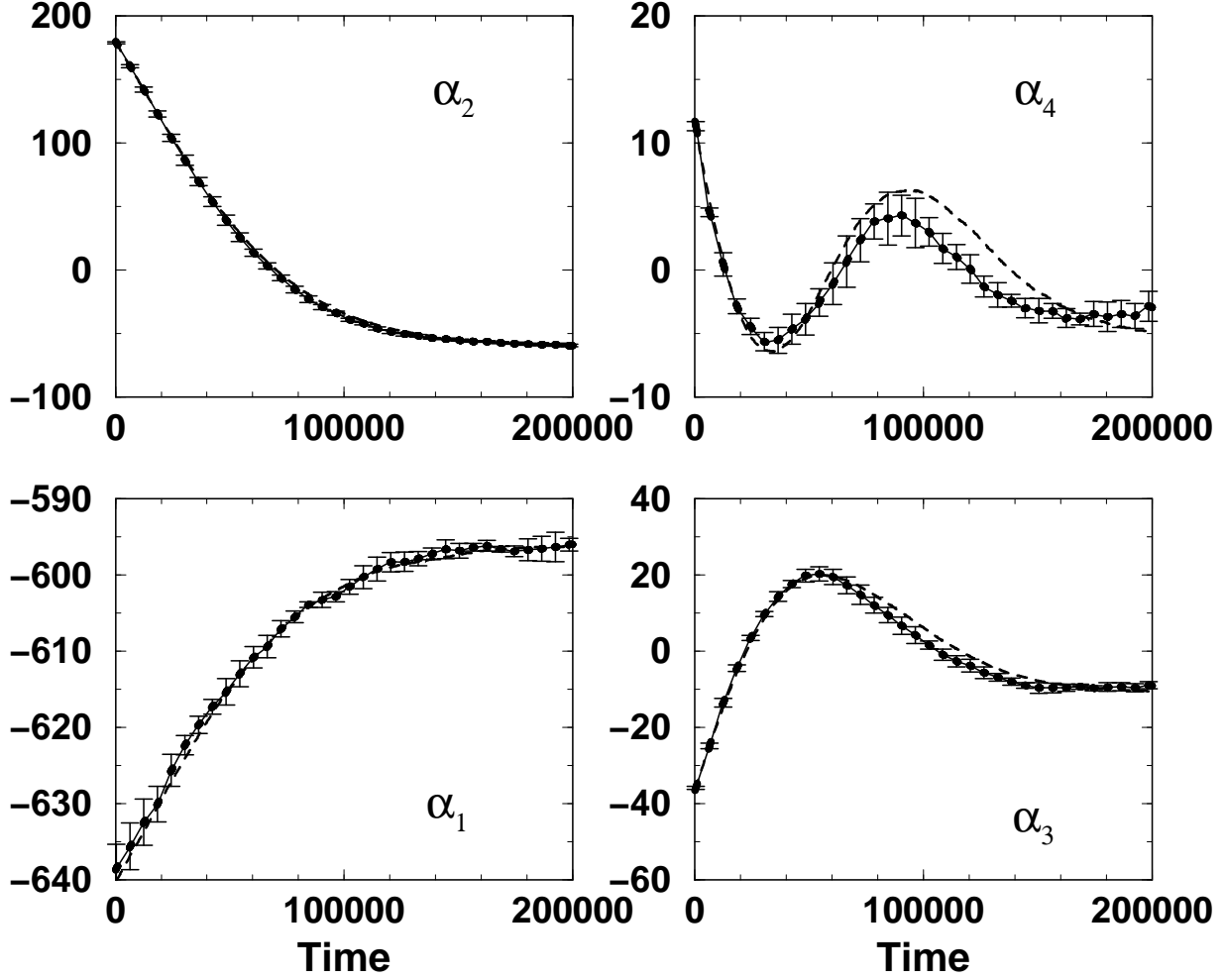


FIG. 8: Coefficients of SVD basis functions: $\alpha^{(r)}(t_i) = \vec{u}_g^{(r)} \cdot \vec{X}_i = \sum_{j=1}^{N_{cells}} u_g^{(r)}(j) X_i(j)$, with CI parameters $(T_{settle}, T_{fit}, T_{proj}) = 10^3 \times (\frac{1}{2}, \frac{1}{2}, 5)$. The points represent averages over $N_{MC} = 5$ realizations, starting from different random number seeds. The error bars, plotted for select points, correspond to the root-mean-square of the distribution of coefficients. The average MC coefficients (dashed line) are shown for comparison.

using local SVD basis functions. In the latter case, since singular value decomposition is applied to a short segment of the MC, we found the higher order local basis functions to be relatively “noisy”; hence, $\{\vec{u}_i^{(1)}, \vec{u}_i^{(2)}\}$ were used in each CI step. Note that the rms of the distribution of errors obtained for CI solutions using local basis function is larger; in this case, the basis functions themselves are also subject to statistical variations. We find that the relative errors using global SVD basis functions are generally smaller than those corresponding to CI solutions obtained using local SVD basis functions. Using either global or local basis functions in the CI step, the smallest relative error is achieved with the first two sets CI of parameters, corresponding to projected time intervals short enough to resolve the macroscopic dynamics of the higher order coefficients of the low-dimensional representation

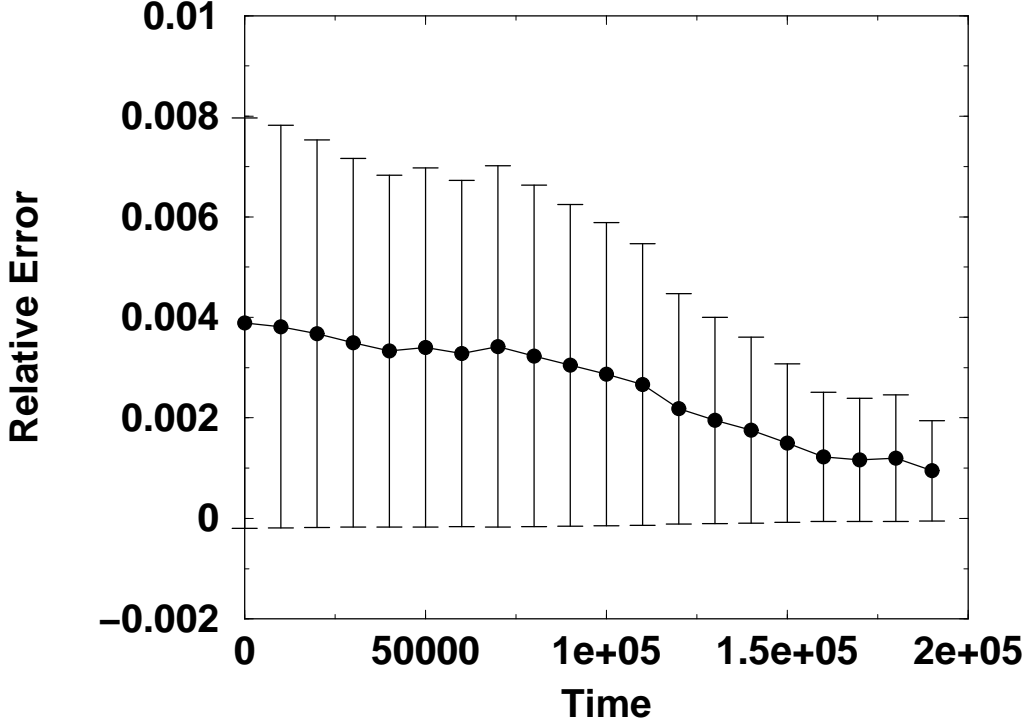


FIG. 9: Relative error given by $\varepsilon_k(t) = \left\{ \sum_{r=1}^4 [\alpha_k^{(r)}(t) - \bar{\alpha}^{(r)}(t)]^2 / \sum_{r=1}^4 [\bar{\alpha}^{(r)}(t)]^2 \right\}^{1/2}$: The points correspond to the average error, obtained over $k = 1, \dots, 10$ MC realizations starting from different random number seeds. The error bars denote the error on the mean, $\sigma_{\bar{\varepsilon}}$.

of the solution.

As a benchmark, in Figure 11 we show the error obtained for $(T_{settle}, T_{fit}, T_{proj}) = 10^3 \times (1, 1, 0)$, using global SVD functions $\{\vec{u}_g^{(r)}\}$, with $r = 1, \dots, 4$ (dotted line) and $r = 1, \dots, 8$ (solid line). These results show the error incurred in restricting the spatial distribution of cell positions to the low dimensional representation given by $\{\alpha^{(r)}\}$, without the contribution from the projective step. First, we note that the maximum error obtained from the restriction to $\{\alpha_g^{(1)}, \dots, \alpha_g^{(4)}\}$ and $\{\alpha_g^{(1)}, \dots, \alpha_g^{(8)}\}$ are comparable, indicating that using a higher dimensional restriction is not significantly advantageous here. Secondly, this error is comparable to the total error in Figure 10(b), which includes projective integration. Given that the total error increases with a longer projective time step, T_{proj} , as shown in Figure 10(c), these results point out that the “optimal” T_{proj} , for which the errors due to the projective time step and restriction are separately comparable, is achieved in Figure 10(b).

Finally, in Figure 12, we compare CI errors using two different reinitialization schemes and find them to be equivalent.

VI. CONCLUDING REMARKS

We have demonstrated, through a coarse projective integration algorithm, that short bursts of appropriately initialized microscopic simulations can be used to simulate the macro-

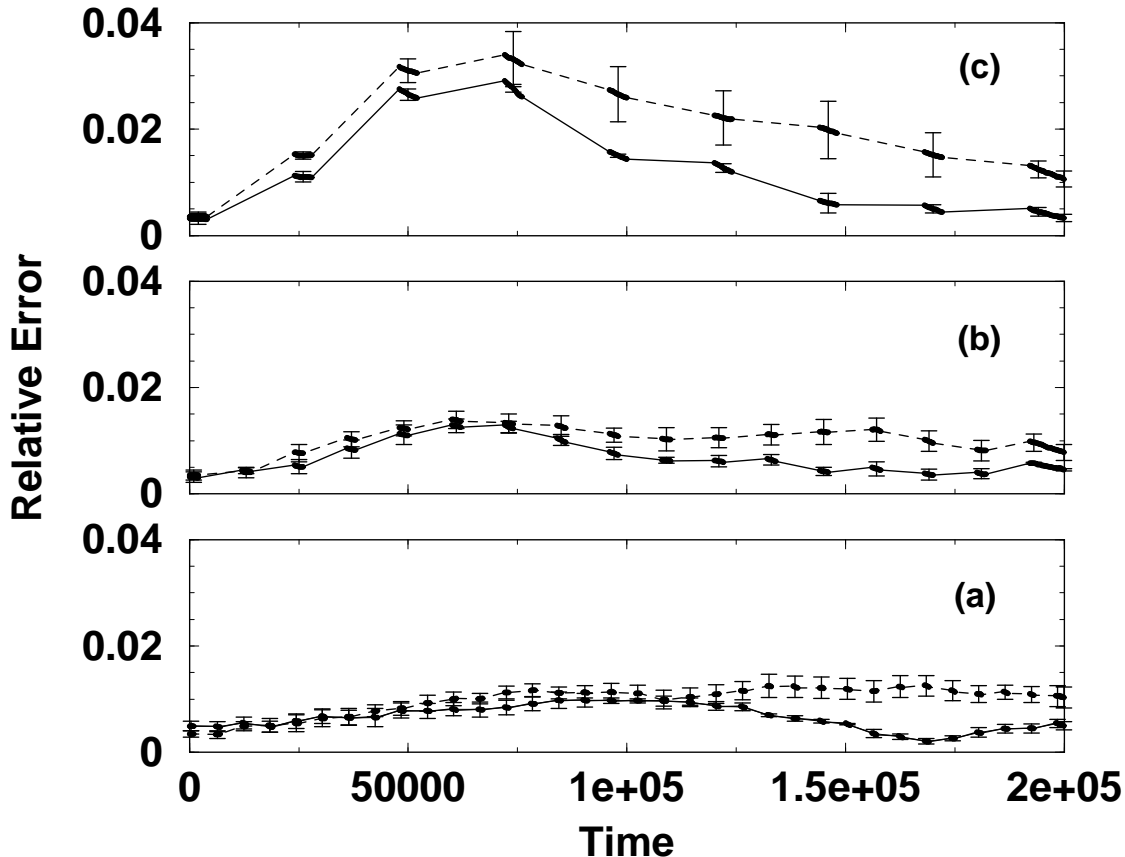


FIG. 10: Relative error given by $\varepsilon(t) = \left\{ \sum_{r=1}^4 [\alpha^{(r)}(t) - \bar{\alpha}^{(r)}(t)]^2 / \sum_{r=1}^4 [\bar{\alpha}^{(r)}(t)]^2 \right\}^{1/2}$, where $\alpha^{(r)}(t)$ are the coefficients of the global SVD basis functions for CI solutions corresponding to parameters $(T_{settle}, T_{fit}, T_{proj}) = 10^3 \times (\frac{1}{2}, \frac{1}{2}, 5)$ (bottom), $(10^3, 10^3, 10^4)$ (middle), and $10^3 \times (2, 2, 20)$ (top). The CI solution at each step was constructed using the first four global basis functions, shown using solid lines, and using the first two local basis functions, shown using dashed lines. The points correspond to averages over $N_{MC} = 5$ realizations starting from different random number seeds. The error bars denote the error on the mean, $\sigma_{\bar{\varepsilon}}$.

scopic evolution of the cell density distribution in bacterial chemotaxis. The outer level of our computational structure was a traditional, continuum Euler integration scheme; the time-derivatives of the cell density field it employed, however, were estimated from short time evolution intervals of the Monte-Carlo description of this process, and not evaluated from a known, macroscopic expression. This approach leads to a general framework for the computer-assisted analysis of systems whose dynamics are given at a microscopic/stochastic “fine” level, but for which we require averaged, macroscopic information.

It is interesting to discuss the benefits and shortcomings of such a procedure. If accurate closed chemotactic equations exist, one should use them instead of the two-tier modeling we propose here. In addition to the insight gained from exact or approximate analytical solutions, computer-aided time-evolution or bifurcation analysis using explicit equations is more efficient than kinetic Monte Carlo simulations. However, if such model equations are not available, our hybrid computational approach can become more economical than long-time direct Monte Carlo simulation. Furthermore, when one is interested in qualita-

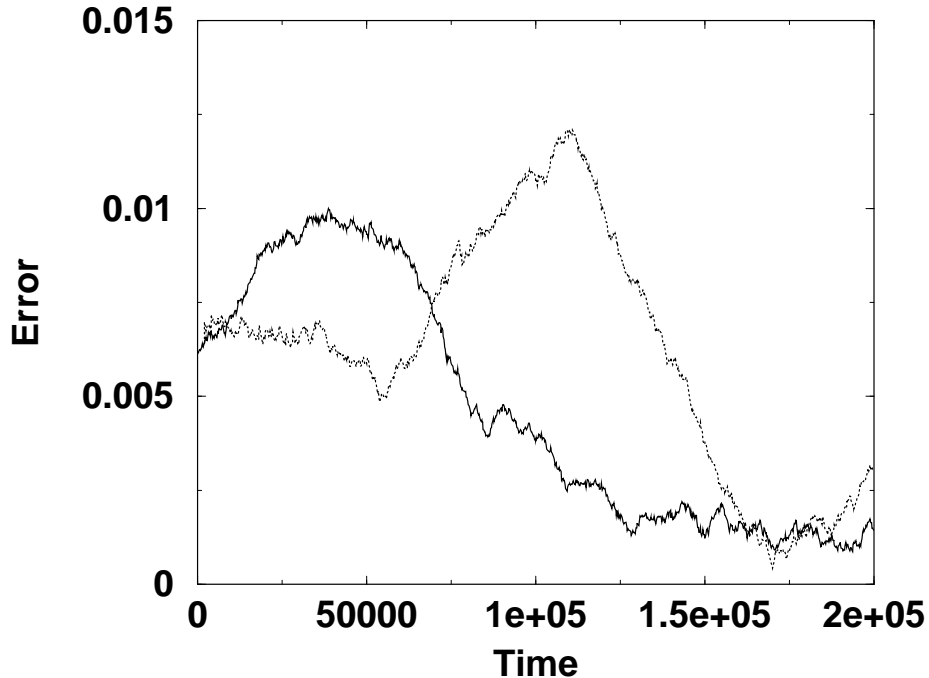


FIG. 11: Relative error given by $\varepsilon(t) = \left\{ \frac{\sum_{r=1}^4 [\alpha_g^{(r)}(t) - \bar{\alpha}^{(r)}(t)]^2}{\sum_{r=1}^4 [\bar{\alpha}^{(r)}(t)]^2} \right\}^{1/2}$ with $(T_{settle}, T_{fit}, T_{proj}) = 10^3 \times (1, 1, 0)$: After each $(T_{settle} + T_{fit})$ interval, the MC evolution is restarted from its low dimensional representation given by $\{\alpha_g^{(1)}, \dots, \alpha_g^{(4)}\}$ (dotted line) or $\{\alpha_g^{(1)}, \dots, \alpha_g^{(8)}\}$ (solid line).

tive transitions or bifurcations of the macroscopic behavior, marginally stable or unstable stationary states may be difficult to identify through direct microscopic simulations, while coarse timestepping holds promise when combined with traditional bifurcation algorithms [7, 9, 29].

It appears, therefore, that a modeler would ultimately gain in obtaining quantitative computational answers efficiently, but perhaps lose in the fundamental understanding of a physical process that macroscopic model equations would offer. Therefore a promising research direction is to use such algorithms to test the validity of explicit closures that assume slaving of certain higher order moments of the evolving distribution to lower order ones. In the chemotaxis context, when signal transduction and corresponding motor response of the cell to an external signal are taken into account as we do here, macroscopic model equations derived systematically from the microscopic description do not exist. The assumption implicit in the coarse integration algorithm was that the macroscopic description closes at the level of the spatial density distribution. In one spatial direction, for example, it would be interesting to learn when this assumption breaks down, requiring separate evolution of right-going, left-going and tumbling cell density distributions.

More generally, we believe that the approach illustrated here for coarse time integration of a Monte Carlo description of bacterial chemotaxis, is broadly applicable with different types of microscopic simulators describing, for example, Brownian, Lattice-Boltzmann, or

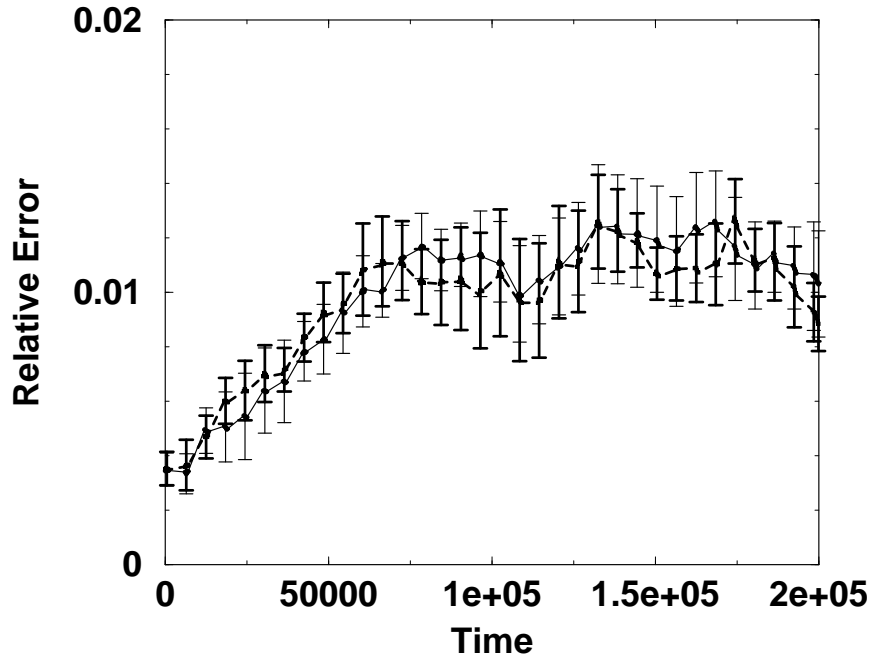


FIG. 12: Comparison of relative errors for CI solutions (using local SVD basis functions) corresponding to two different flagellar reinitialization schemes. The signal transduction variables were initialized to their local equilibrium values, $\bar{u}_j = \{0, f(S(x_j))\}$. In one case, all flagella were started in the CW state, shown in the thin solid line; in the second case, all flagella were started in the CCW state, with those cells to the left (right) of the chemoattractant peak running right (left), shown in the thick dashed line. The points correspond to averages over $N_{MC} = 5$ realizations starting from different random number seeds. The error bars denote the error on the mean, $\sigma_{\bar{\epsilon}}$.

molecular dynamics, and leading to emergent macroscopic dynamic behavior. Such a hybrid scheme allows efficient simulation of the macroscopic behavior, and may provide insight into macroscopic model equations.

ACKNOWLEDGEMENTS

The work reported here was supported by the Princeton Council on Science and Technology Fellowship (SS), NIH Grant #GM29123 and NSF Grant #DMS 0074043 (HGO), and AFSOR (Dynamics and Control) and NSF-ITR grants (CWG and IGK).

-
- [1] V. B. Shenoy, R. Miller, E. B. Tadmor, D. Rodney, R. Phillips and M. Ortiz, *J. Mechanics and Phys. Solids* **47**, 611 (1999).
 - [2] A. L. Garcia, J. B. Bell, W. Y. Crutchfield and B. J. Alder, *J. Comp. Phys.* **154**, 134 (1999).
 - [3] I. G. Kevrekidis, C. W. Gear, J. M. Hyman, P. G. Kevrekidis, O. Runborg and K. Theodoropoulos, submitted to *Comm. Math. Sciences*, August 2002; Can be obtained as

- physics/0209043 at arXiv.org.
- [4] K. Theodoropoulos, Y. H. Qian and I.G.Kevrekidis, *Proc. Natl. Acad. Sci.* **97**, 9840 (2000).
 - [5] C. W. Gear, I. G. Kevrekidis and C. Theodoropoulos, *Comp. Chem. Engng.* **26**, 941 (2002).
 - [6] J. Li, P. G. Kevrekidis, C. W. Gear and I.G.Kevrekidis, *SIAM MMS*; Can be obtained as physics/0212034 at arXiv.org.
 - [7] A. G. Makeev, D. Maroudas, and I. G. Kevrekidis, *J. Chem. Phys.* **116**, 10083 (2002).
 - [8] A. G. Makeev, D. Maroudas, A. Z. Panagiotopoulos and I. G. Kevrekidis, *J. Chem. Phys.* **117**, 8229 (2002).
 - [9] C. Siettos, M. D. Graham and I. G. Kevrekidis, *J. Chem. Phys.* **118**, 10149 (2003); Can be obtained as cond-mat/0211455 at arXiv.org.
 - [10] G. Hummer and I.G.Kevrekidis, *J. Chem. Phys.* **118**, 10762 (2003); Can be obtained as physics/0212108 at arXiv.org.
 - [11] M. Melchior and H. C. Oettinger, *J. Chem. Phys.* **103**, 9506 (1995).
 - [12] M. Melchior and H. C. Oettinger, *J. Chem. Phys.* **105**, 3316 (1996).
 - [13] H. G. Othmer and T. Hillen, *SIAM JAM* **62**, 1222 (2002).
 - [14] R. M. Macnab and D. E. Koshland, *Proc. Natl. Acad. Sci.* **69**, 2509 (1972); S. M. Block, J. E. Segall, and H. C. Berg, *J. Bacteriol.* **154**, 312 (1983); J. E. Segall, S. M. Block, and H. C. Berg, *Proc. Natl. Acad. Sci.* **83**, 8987 (1986); J. B. Stock and M. G. Surette in *Escherichia coli and Salmonella, Cellular and Molecular Biology*, eds. F. C. Neidhardt *et al.*, 1103 (1996); J. Stock and S. Da Re, *Encyclopedia of Microbiology* **1**, 772 (2000).
 - [15] N. Barkai and S. Leibler, *Nature* **387**, 913 (1997).
 - [16] P. A. Spiro, J. S. Parkinson and H. G. Othmer, *Proc. Natl. Acad. Sci.* **94**, 7263 (1997).
 - [17] C. J. Morton-Firth and D. Bray, *Journal of Theoretical Biology* **192**, 117 (1998).
 - [18] H. C. Berg and E. M. Purcell *Biophysical Journal* **20**, 193 (1977).
 - [19] H. G. Othmer and P. Schaap, *Comments on Theoretical Biology* **5**, 175 (1998).
 - [20] S. M. Block, J. E. Segall and H. C. Berg, *Journal of Bacteriology* **154**, 312 (1983).
 - [21] R. M. Macnab, in *Two-component Signal Transduction*, J. A. Hock and T. J. Silhavy eds., 181 (1995).
 - [22] P. Cluzel, M. Surette and S. Leibler, *Science* **287**, 1652 (2000).
 - [23] B. E. Scharf, K. A. Fahrner, L. Turner and H. C. Berg, *Proc. Natl. Acad. Sci.* **95**, 201 (1998); L. Turner, A. D. T. Samuel, A. S. Stern, and H. C. Berg, *Biophysical Journal* **77**, 597 (1999).
 - [24] A. Ishihara, J. E. Segall, S. M. Block, and H. C. Berg, *J. Bacteriol.* **155**, 228 (1983).
 - [25] F. W. Dahlquist, *Science's STKE* (2002), http://www.stke.org/cgi/content/full/OC_sigtrans;2002/132/pe24; D. Bray, *Proc.Natl. Acad. Sci.* **99**, 7 (2002).
 - [26] C. W. Gear, "Projective Integration Methods for Distributions", NEC TR 2001-130, 26 November 2001.
 - [27] E. N. Lorenz, Tech Rep 1, MIT, Department of Meteorology, Statistical Forecasting Project, Cambridge, MA (1956).
 - [28] P. J. Holmes, J. L. Lumley and G. Berkooz, *Turbulence, Coherent Structures, Dynamical Systems and Symmetry*, (Cambridge University Press, 1996).
 - [29] R. Rico-Martinez, C. W. Gear and I. G. Kevrekidis, submitted to *J. Comp. Phys.*; Can be obtained as nlin.CG/0307016 at arXiv.org.